



High strength welding of Ti to stainless steel by spot impact: microstructure and weld performance

Jianxiong Li¹ · Benjamin Schneiderman² · Shaopin Song³ · Sarah M. Gilbert² · Anupam Vivek¹ · Zhenzhen Yu² · Pingsha Dong³ · Glenn S. Daehn¹

Received: 17 April 2020 / Accepted: 18 May 2020 / Published online: 27 May 2020
© Springer-Verlag London Ltd., part of Springer Nature 2020

Abstract

Vaporizing foil actuator (VFA) spot welding, a type of spot impact welding, was used to weld a titanium alloy (Ti-1.2ASn) to a stainless steel (436 SS). The interfacial microstructures and fracture surfaces were characterized using scanning electron microscopy (SEM). Lap shear tests that strained the samples to failure with digital imaging correlation (DIC) were conducted to study the mechanical performance of these welds. A mesh-insensitive structural stress method was used to understand the stress distribution and model the failure modes of VFA welds in ABAQUS. Despite experimental scatter in this developing joining method, most samples failed through the base metal, but multiple failure modes coexisted, including interface failure. These failure modes were used to classify the results. The failure process can be best understood through the lens of the spatial variation that is natural in this type of weld. The center is naturally unwelded, and there is an annulus of high strength material surrounding this unwelded zone that has a wavy morphology. The mesh-insensitive structural stress method could naturally provide a link between the joint structure and the mechanical properties of the spot impact welds. This could show that despite varied failure modes and nugget strength, strength itself is not usually affected adversely by the size of the central unbonded zone.

Keywords Titanium alloy · Stainless steel · Impact spot welding · Peel tests · Digital imaging correlation · Mesh-insensitive structural stress method

1 Introduction

Titanium and its alloys offer good corrosion resistance, high specific strengths, and reliable mechanical properties at elevated temperatures. These alloys have broad applications in automotive, aerospace, and oil industries as well as aviation, nautical, and petrochemical markets [1]. To provide greater design flexibility and often lower the cost of the product,

titanium and its alloys have been welded to steel to achieve high performance and lightweight structures in both exhaust and aircraft actuation system components [2].

Welding of Ti to SS is extremely difficult. Direct fusion welding of Ti alloy to SS is undesirable due to the notable mismatch in physical properties, excessive formation of brittle intermetallic compounds (IMC), and excessive distortion and residual stresses imposed during welding. Advanced welding processes have been developed to join Ti alloys to SS. These processes can be classified into two groups: high energy density (HED) beam welding processes and solid-state welding processes. HED beam welding processes entail laser beam welding [3] and electron beam welding [4]. Solid-state welding methods include friction welding [5], friction stir welding [6], diffusion bonding [7], and explosive welding [8–11].

To prevent the excessive formation of IMC, interlayers are often utilized to join Ti alloy and SS in laser beam welding and electron beam welding. AISI 316L SS was welded to Ti6-Al4-V alloy via a pure vanadium interlayer by laser beam welding in [3]. In this process, the undesirable sigma phase

Electronic supplementary material The online version of this article (<https://doi.org/10.1007/s00170-020-05506-4>) contains supplementary material, which is available to authorized users.

✉ Jianxiong Li
li.8266@osu.edu

¹ Department of Materials Science and Engineering, The Ohio State University, 2041 College Road, Columbus, OH 43210, USA

² Department of Metallurgical and Materials Engineering, Colorado School of Mines, Golden, CO 80401, USA

³ Department of Naval Architecture and Marine Engineering, University of Michigan, Ann Arbor, MI 48109, USA

forming between iron and vanadium was prevented; however, the ultimate tensile strengths (UTS) of joints were low due to excessive heat supply and annealing. Tomashchuk et al. [4] studied the microstructure and mechanical properties resulting from dissimilar electron beam welding of Ti alloy to SS via a copper interlayer. The beam offset had a noticeable influence on the formation of IMC. Fe_2Ti accumulated considerably at the interface when the beam offset was on the titanium side. These two HED beam processes can, to some extent, prevent the excessive formation of IMC because of the use of interlayers. However, the experimental conditions are rigid and not cost-effective. This means HED beam processes with interlayers are not desirable for joining Ti alloys and SS. Solid-state welding methods are thus preferable for joining these two.

Direct friction welding of Ti alloy to SS has not been shown to produce reliable joints. Muralimohan et al. [5] studied the properties of friction-welded Ti-SS joints with a nickel interlayer. The highest joint strength was only 66% of the UTS of titanium alloy and the tensile fracture surfaces exhibited the river-like patterns of brittle fracture even at optimal conditions. Friction stir welding parameters were adjusted to achieve dissimilar lap joints between CP-Ti to 304 stainless steel [6]. These joints' shear strengths were only 73% of the UTS of commercially pure titanium (CP-Ti). These joints fractured at the intermetallic-based joint interface due to the degradation of the heat-affected zone (HAZ) and thermo-mechanically affected zone induced by friction heat. Kundu and Chatterjee [7] performed diffusion bonding between Ti alloy and 304 SS using a nickel interlayer in the temperature range of 800 to 950 °C for 1 h under a 3-MPa load in a vacuum chamber. Nickel can inhibit the diffusion of Ti to SS side from 800 to 900 °C; however, Ti crosses the nickel layer to form Fe-Ti IMC at 950 °C. Diffusion bonding can be time-consuming due to the low heating rate and subsequent cooling process. This process is, therefore, not efficient for high production rates.

Impact welding has been growing in popularity as a method for joining dissimilar alloys. Impact welding methods include explosion welding, magnetic pulse welding, laser impact welding, and vaporizing foil actuator welding. These are all high-velocity impact welding methods and less time consuming than other solid-state welding methods. Chu et al. [10] studied the microstructure and mechanical properties of titanium and steel interfaces prepared by explosive welding. The melted zone, mainly resulting from the trapped jet, is dominated by Fe_2Ti intermetallics surrounded by a mixture of FeTi and Fe. Mousavi et al. [11] investigated explosive welding of CP-Ti and AISI 304 SS. At low explosive loads, the interfaces between these two alloys were flat with no IMC formation. When the explosive loads were high, however, brittle intermetallic phases such as Fe_2Ti , $\text{Fe}_2\text{Ti}_4\text{O}$ and Cr_2Ti were identified in the interfaces. Explosion-welded joints can present

solid-state joining with reliable mechanical properties. The possible workpiece dimensions are, however, on a large scale on the order of meters. This process is therefore not suitable for small-scale joining [12]. Furthermore, the application of this process is limited due to operation safety issues and environmental concerns.

Magnetic pulse welding (MPW) has been recently used to join dissimilar metals. In this process, magnetic pressure created by electromagnetic coils was utilized to drive the flyer plate or tube towards the target. But the problem associated with this method is that the materials joined must be highly conductive, or else they cannot be driven by magnetic repulsion. Also, the coil life is limited at high discharge energies and must be replaced periodically [13]. Laser impact welding can only provide several joules and thus has insufficient energy to drive rigid metal combinations such as Ti alloy and SS.

Vaporizing foil actuator welding (VFAW) involves vaporizing a thin aluminum foil with a high current, creating a high-pressure plasma to accelerate the flyer towards the target to create an impact weld. Hahn et al. [12] compared MPW and VFAW by welding 5XXX series aluminum alloy at the same energy inputs. The results showed that no magnetic pulse welds were achieved, while every VFAW experiment yielded strong welds. These welds fractured in the joining elements instead of in the weld seam during tensile tests. This was because the VFAW method created higher impact velocity at the same input energy. Also, the irrelevancy of workpiece conductivity and lack of an issue with tool life constitute another two advantages of VFAW over MPW. Vivek et al. [14] studied VFAW of Al-Cu, Al-Mg, and CP-Ti to 1018 steel. The results show that VFAW can be utilized to weld different metal combinations with reliable mechanical properties.

In a recent work [15], the relation of process to microstructure of spot impact welding between Ti and SS was explored. In this work, the microstructure characteristics and weld performance were studied. Interfacial microstructure and fracture surface after lap shear tests were characterized. The influence of interfacial waviness on failure modes was examined. Mechanical responses of these welds were studied systematically from peak load to absorbed energy during the processes to failure modes. Finally, failure modes in impact spot welds were modeled using mesh-insensitive structural stress method for the first time. The possible mechanisms for these failure modes were discussed.

2 Experimental

Impact welds were created between titanium and stainless steel. Ti-1.2ASN (Ti-0.5Al-0.45Si-0.2Nb), supplied by KOBE STEEL, LTD., was selected as the flyer material, entailing β -transus temperature of 907 °C, density of 4.5 g/cm³, and ultimate tensile strength (UTS) of 430 MPa. 436

SS (Fe-16Cr-1Mo-1Mn-0.5Nb-0.12C), a ferritic stainless steel, was selected as the target material, entailing a density of 7.7 g/cm^3 and UTS of 538 MPa. SS sheets were preformed to a dimple shape as shown in Fig. 1b. The dimple provides a standoff distance of 2 mm to create the collision angle and distance for acceleration that is required for an impact weld. VFA spot welding largely followed procedures published previously [16, 17]. Figure 2 shows the schematic of VFA spot welding process. A 0.0508-mm-thick spot-type aluminum foil actuator was placed on top of the Ti flyer as shown in Fig. 2a, b. The geometry of the actuator was designed so that the narrowest “active” area vaporizes first due to increased current density in that area. The vaporized aluminum pushes the Ti flyer towards the SS target with a high pressure (up to several GPa) [18] as shown in Fig. 2c. This is the first contact between Ti and SS is in the center of the weld, at which the collision speed is high, and the collision angle is zero, resulting in no weld formation in this zone. As the collision front travels outward from the center, the collision angle increases, a flat interface with continuous melting is adjacent to the center, a wavy interface with discontinuous melting, and a wavy interface with no melting form were shown in Fig. 2d. Expelled or jetted material is also collected in the edges of the dimple. These interfacial microstructures will be studied in detail in Section 4.1.

The energy source used in this work was a capacitor bank custom-built at The Ohio State University with a total capacitance of $52 \mu\text{F}$, an inductance of 350 nH, and a resistance of $3.1 \text{ m}\Omega$. The maximum charging energy of the capacitor bank is 3 kJ associated with a charging voltage of 10.74 kV and a current rise time of $7 \mu\text{s}$. Input energies ranging from 2.0 to 2.6 kJ were used in this study. One initial intent of the broad study was to find the effect of discharge energy on the structure and properties of the welds that were created. However, normal experiment-to-experiment variation (often due to manual foil placement) was a more significant factor than energy input. Therefore, samples were classified according to failure mode in testing.

Interfacial microstructure and fracture surface were characterized by scanning electron microscopy (SEM). The chemical compositions of the trapped jet zone were evaluated by energy-dispersive X-ray spectroscopy (EDS). Lap shear tests and peel tests were carried out using MTS 831.10 load frame at a displacement rate of 0.1 mm/s, during which the joints were pulled at both ends until failure. Five samples were lap shear tested for each input energy level. DIC method was used to monitor strain partitioning in the spot weld during tensile-shear testing. For DIC, a speckled pattern was applied to the surface of the tensile sample, by using white spray paint to create a uniform background and black spray paint to generate contrasting speckles. The speckles should have a slight variation of diameter over the desired area and be separated enough that roughly 3 to 5 speckles can be detected per pixel by the DIC camera. Due to the geometry of the welds, the DIC patterns, and therefore the strain concentration maps, were on the outer surfaces of the weld. Images of the pattern were taken every 15 s during testing using TQS Snap software and analyzed by Aramis software. Aramis uses the speckled pattern from the images to track deformation in the joints and correlates that to strains at each location.

3 Traction structural stress method

To understand the effects of VFA spot joint characteristics on the weld strength and failure modes, the mesh-insensitive traction-based structural stress method was used. The general concept of this method on fatigue evaluation of various types of welded joints was first proposed by Dong [19], and its capability in consolidating a large amount of fatigue data of spot welds has been demonstrated in [20]. Recently, this method has been proven effective in strength evaluation of welded joints as well [21]. In this study, the traction-based structural stress method will be used to understand the varied failure modes of VFA spot welds. Due to space limitations, only

Fig. 1 Configuration of lap shear VFA spot joints. **a** Top view and dimensions; **b** Side view and dimensions

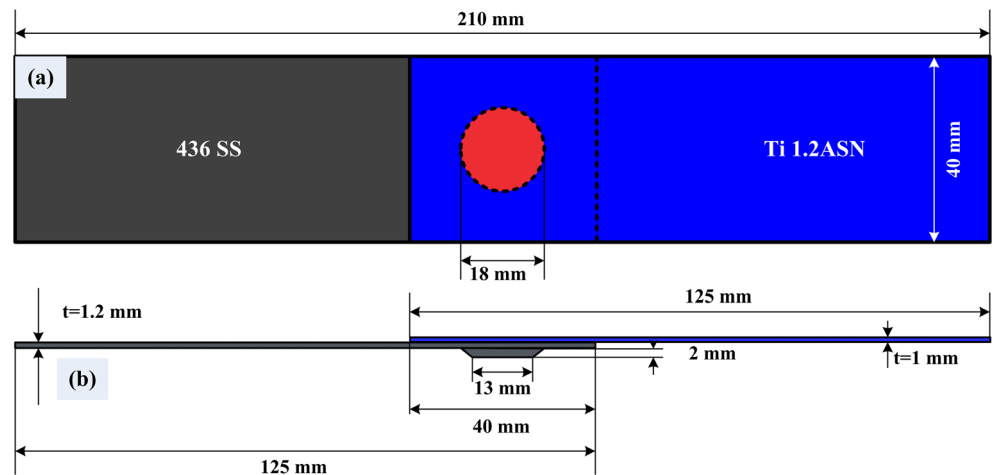
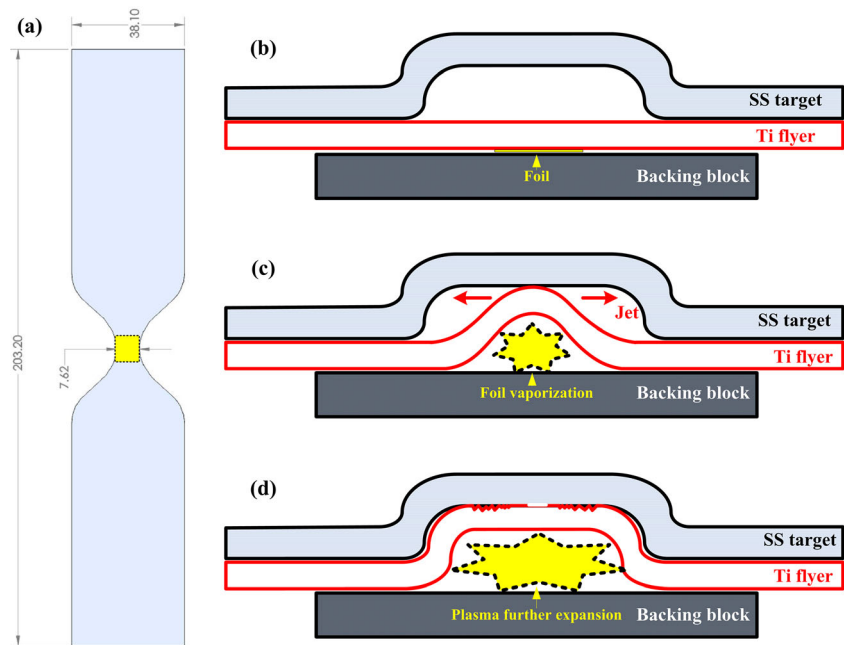


Fig. 2 Schematic of VFA spot welding process. **a** Geometry of vaporizing foil actuator; **b** Initial setup before welding; **c** First contact between flyer and target; **d** Final weld geometry



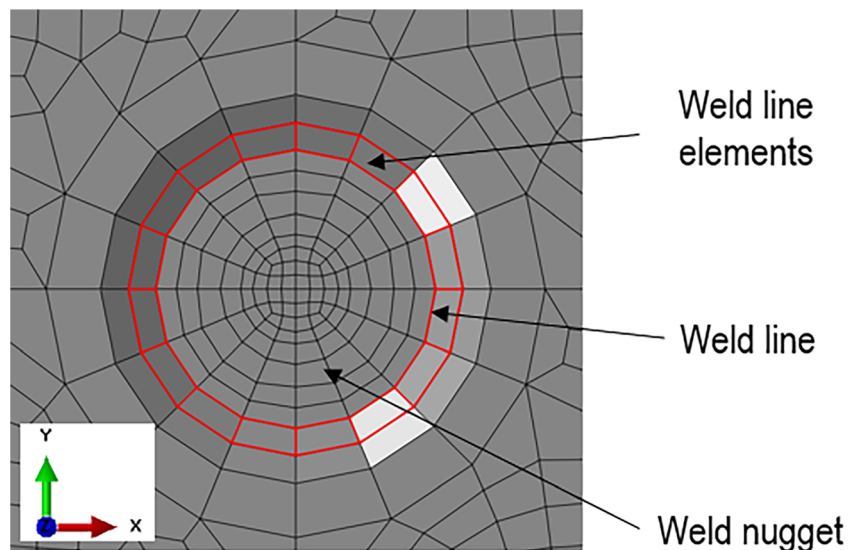
the necessary procedures required for analyzing the VFA spot joint specimens are briefly described below. Further detailed discussions on the mechanical basis and generalized computation procedures of the traction-based structural stress method can be found in recent publications [19–24].

3.1 Structural stress calculation

For the structural stress calculation, the specimen for VFA spot joint was modeled with 3D solid elements using ABAQUS. Figure 3 shows a representative finite element mesh around a VFA weld nugget. The structural stress was calculated along the weld line using the weld line elements as highlighted in Fig. 3. The weld line is defined as the periphery

of the weld nugget, which is the inner circle of the highlighted elements. The normal direction (z -direction) of those elements is used to calculate the structural stress for through-thickness sheet failure. The weld nugget in the finite element model is the area surrounded by the weld line elements. The nodal forces from the weld line elements at the weld line nodal positions are extracted and fed into the simultaneous matrix equation [20–22] for solving the line forces and line moments with respect to the mid-surface of the sheet. The corresponding structural stress can then be calculated at each nodal position along the weld line by dividing the line force by the sheet thickness for membrane stress σ_m and line moment by section modulus for bending stress σ_b . The details in calculating σ_m and σ_b can be found in [20–22].

Fig. 3 3D solid finite element mesh around a VFA weld nugget



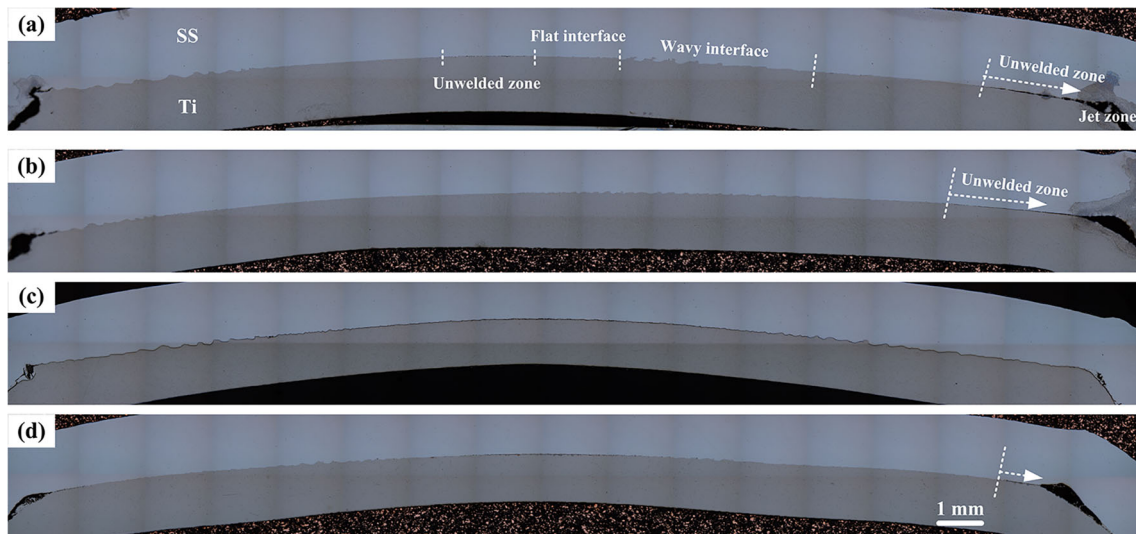


Fig. 4 Interfacial macrostructure overview at different input energy level from 2.0 to 2.6 kJ. **a** 2.0 kJ; **b** 2.2 kJ; **c** 2.4 kJ; **d** 2.6 kJ. A typical spot impact weld includes an unwelded zone in the weld center, a flat interface, a wavy interface, and a trapped jet zone at the edge

3.2 Effective structural stress parameter for test specimens

In lap shear tests, membrane stress σ_m is the dominant stress component due to excessive plastic deformation [21]. Bending stress σ_b does not have the full effect since the limit condition is $\frac{2}{3}\sigma_b$ when considering a fully yield condition for the section in which the top half fiber is subjected to full tensile yield stress and

the bottom half fiber is subjected to full compressive yield stress. To combine the membrane stress σ_m and bending stress σ_b to form an effective structural stress parameter σ_e for correlating tensile test data, the elastic core concept developed in [22] is borrowed to derive such a parameter. For a section subjected to a combined σ_m and σ_b that exceeds the material yield strength S_y , the stress distribution must be re-distributed to satisfy equilibrium conditions (i.e., force and moment balances) if considering

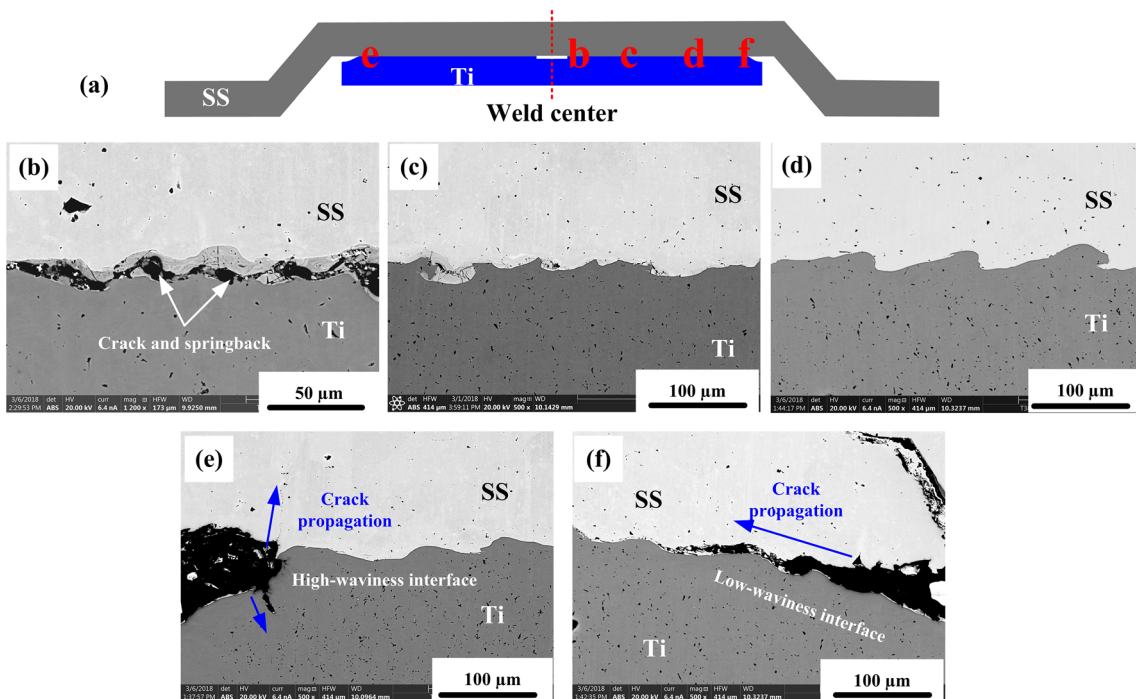


Fig. 5 Microstructure analysis of a spot joint welded at 2.2 kJ after nugget pullout failure in the titanium side (N-Ti). **a** Schematics of Ti/SS impact spot weld after Ti nugget pullout failure; **b** Melting layer rebound in area near the weld center; **c** Wavy interface with discontinuous melting; **d**

Wavy interface with no melting; **e** Fracture position at left edge; **f** Fracture position at right edge. Arrows in **e** and **f** stand for the crack propagation direction during lap shear tests

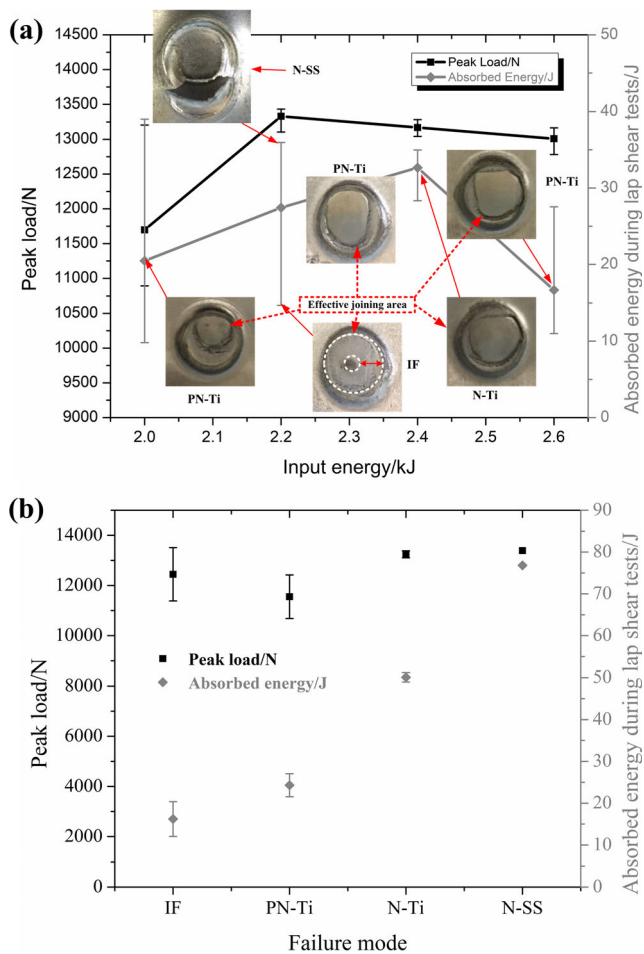


Fig. 6 Lap shear testing results. **a** Effect of input energy on peak loads and absorbed energies during lap shear testing; **b** Results classified as failure modes. The error bars in **b** stand for the standard deviations of each failure mode. For N-SS failure mode, only one case is found and that is why there is no error bar in this data set

elastic-perfectly-plastic material response. The characteristic of the resulting stress distribution is the presence of the elastic core. If the section is fully plastic which is similar to the tensile test condition, the elastic core is vanished. Then the critical condition of the elastic core existence or the limit condition that a section can take on the maximum combination of σ_m and σ_b is [24]:

$$\left(\frac{\sigma_m}{S_y}\right)^2 + \frac{2}{3}\left(\frac{\sigma_b}{S_y}\right) = 1 \quad (1)$$

Under the limit condition described by Eq. (1), substitute S_y to the effective stress σ_e and solve for σ_e in terms of σ_m and σ_b :

$$\sigma_e = \frac{\sigma_b + \sqrt{9\sigma_m^2 + \sigma_b^2}}{3} \quad (2)$$

σ_e is the effective stress under the combination effect of σ_m and σ_b . After calculating the effective stress σ_e for the

potential failure locations, σ_e can be served as a criterion for ranking those locations to identify the most possible one. Furthermore, σ_e has the capability to correlate the tensile test data since it represents the effective stress state under limit condition during lap shear tests.

4 Results

4.1 Interfacial macrostructure and microstructure

In the previous work [15], the effect of input energy on the impact velocity is insignificant. The insignificant variation in impact velocity results in insignificant changes in microstructures. Figure 4 shows the interfacial macrostructures at different input energy level. As studied in Fig. 2, a typical spot impact weld entails an unwelded zone in the center, a flat interface, a wavy interface, and a trapped jet zone at the edges. However, as shown in Fig. 4, an unwelded zone was also shown close to the edges of welds made at 2.0, 2.2, and 2.6 kJ, and a flat interface was located right after wavy interface. The formation of these zones is likely due to the uneven distribution of plasma pressure when the aluminum foil is manually placed. The unwelded zone close to the trapped jet zone presents high stress concentration, resulting in partial pullout failure that will be studied in Section 4.2. As input energy increases, the size of the unwelded zone close to the trapped jet zone decreases. This corresponds to the partial nugget pull-out failure at 2.0 kJ and nugget pullout failure at 2.4 kJ, as shown in Fig. 6. The detailed microstructural characterization can be seen in the previous work [15]. The interfacial microstructure of a typical spot weld after lap shear tests will be studied in Fig. 5.

Figure 5 shows the interfacial microstructure of an impact spot weld after Ti nugget pullout failure. A typical impact spot weld entails five regions including unbonded zone in the center, flat interface with continuous melting, wavy interface with discontinuous melting (Fig. 5c), wavy interface with no melting (Fig. 5d), and trapped jet zone. The trapped jet zone was not shown here due to the pullout failure of the weld. Interfacial waviness becomes higher as the collision propagates from the center unbonded zone towards the ends, due to the corresponding increase in collision angle.

During lap shear tests, cracks initiate at the interfacial regions near the trapped jet zone due to a high stress concentration and likely poor mechanical properties of the weld in this region. High-waviness interfaces provided larger bonding area and stronger metallurgical bonding with possible mechanical interlocking and thus impeded the crack propagation through the interface. This forced the cracks to go through the Ti flyer in the thickness direction (Fig. 5e). As shown in Fig. 5f, the cracks initiated and propagated along the low-waviness interface and went further until they meet high-waviness interfaces. In

areas near the unbonded zone (Fig. 5b), cracks occurred in low-waviness interfaces which melted, mixed, and re-solidified. This mixed zone likely has very poor toughness. Since the unbonded zones are in the center of the joints, they have an insignificant effect on the tensile-shear strength. The zones near the center that likely melted, mixed, and formed brittle intermetallics similarly do not necessarily affect overall behavior as they are protected by the strong ring in this failure mode.

4.2 Lap shear testing results

Examination of the tensile samples showed that several distinct failure modes were possible, and the relative frequency of these modes was only loosely correlated with discharge energy, as shown in Fig. 6a. Also, these all had relatively similar peak loads, indicating these modes were in relatively even competition with one another. The peak loads and energy absorbed in the tensile test are correlated with failure modes in Fig. 6b. The modes found are classified as:

- IF—interfacial fracture,
- PN-Ti—partial pullout failure on titanium,
- N-Ti—nugget pullout failure on titanium, and
- N-SS—nugget pullout failure on stainless steel.

These are operationally defined in Fig. 6a. IF, PN-Ti, and N-Ti are the dominant failure modes for samples welded at this input energy range. For the total 20 samples being tested, there are 4 samples fracturing as IF mode, 6 samples exhibiting PN-Ti mode, 9 samples showing N-Ti mode, and

1 sample exhibiting N-SS mode. Pullout failure (N-Ti and PN-Ti) and interfacial failure modes are considered the dominant failure modes. The data in Fig. 6 shows that while peak load varied little with failure mode, average absorbed energy during lap shear testing increases when failure mode changes from IF to NP. The remaining Ti base metals in partial nugget pullout and nugget pullout modes denote the effective joining area (EJA) of welds. Nugget pullout failure mode presents larger EJA than the partial pullout failure mode and thus, the former has larger absorbed energy than the latter. When the fracture occurred in the SS base metal in the thickness direction, the absorbed energy was larger than those in other cases since the EJA was the whole button and the peak load was dominated by the UTS of 436 SS base metal.

Stress concentrated along the circumference of the button due to the shape of the bonded area and thinning occurred after impact. This stress concentration was captured by DIC performed in situ during tensile testing, which likely influences the failure modes of the spot impact welds during lap shear testing. Samples that failed by base metal failure, as shown in Fig. 7b, exhibited similar strain distribution patterns at earlier deformation stages to those failed through the weld interface (Fig. 7a). The distinction is that in the base metal failure samples, deformation continues to build up in the Ti base metal adjacent to the weld until failure.

4.3 Fracture surface characterization

Figure 8 shows the macrostructure and microstructure of a sample that failed by purely interfacial fracture. The unbonded

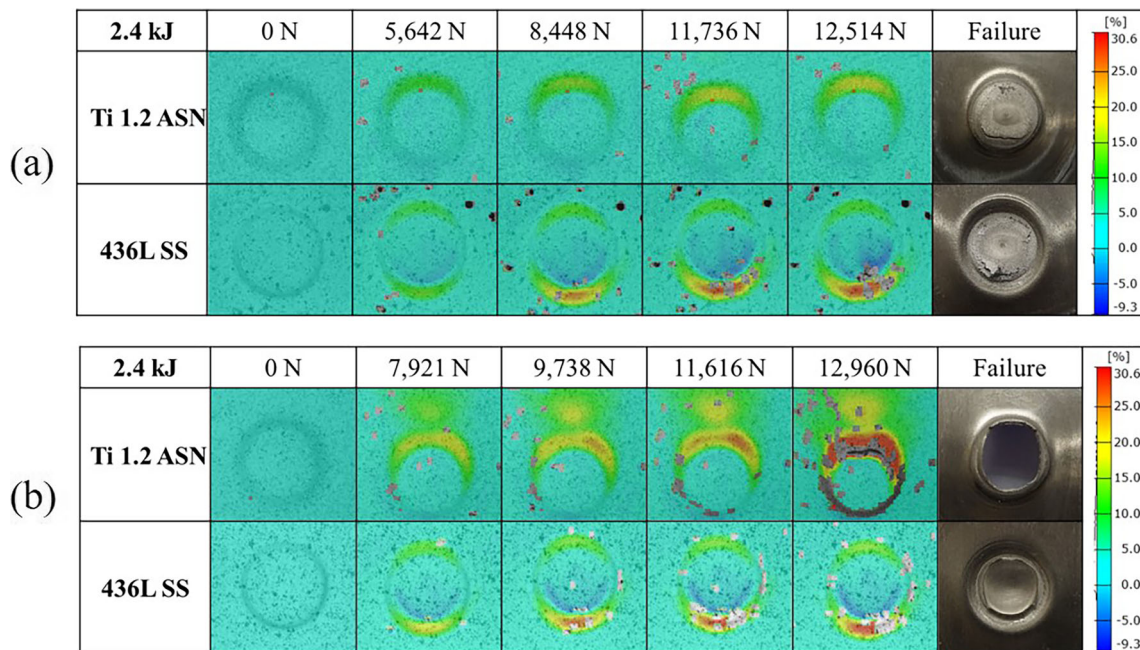


Fig. 7 DIC results in which the color map represents normal strain in the y -direction for tensile samples that exhibited interfacial fracture (a) and nugget pullout failure on Ti side (b)

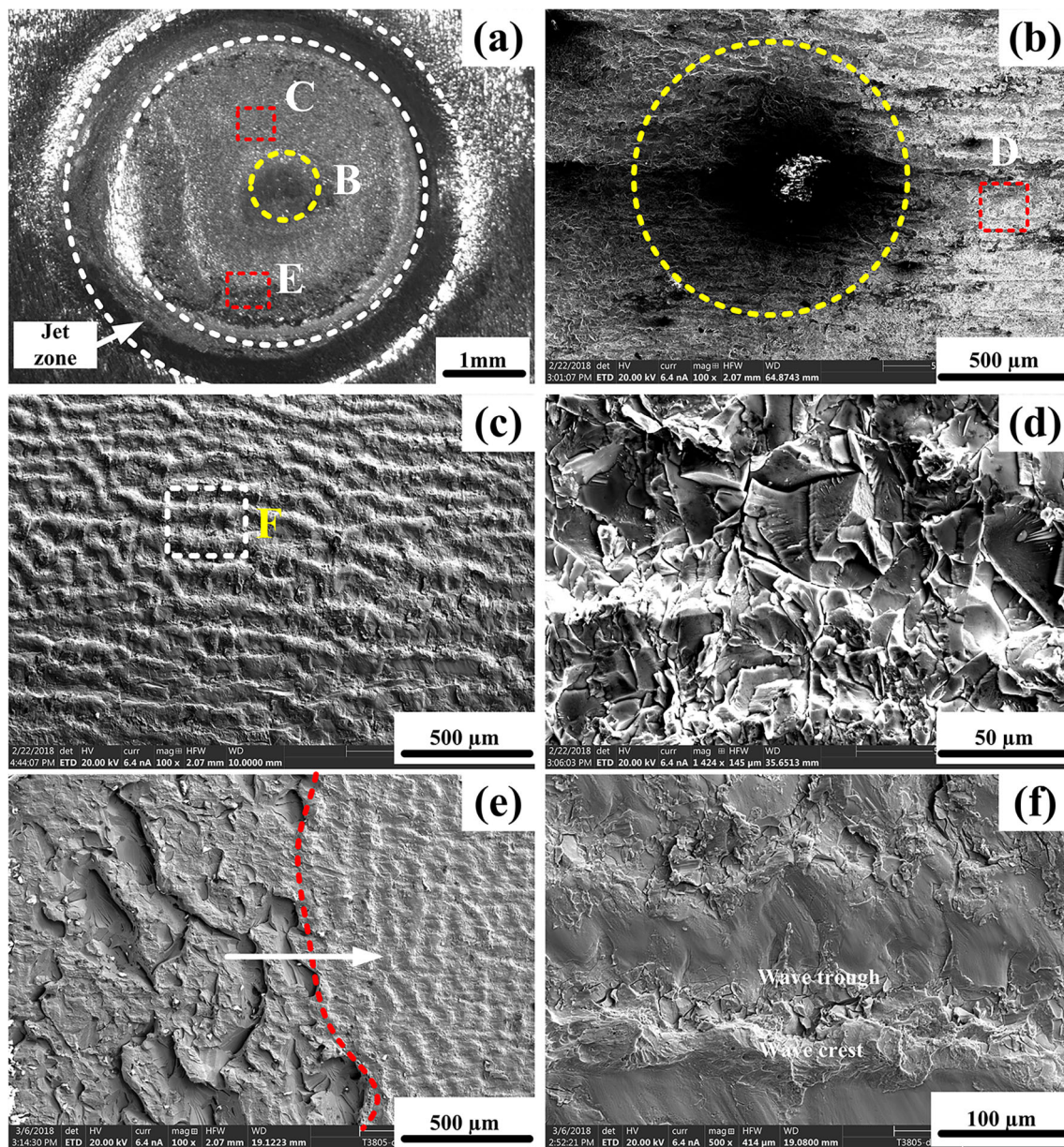


Fig. 8 Microstructure analysis of a spot joint welded at 2.2 kJ with typical interfacial fracture (type IF). **a** Macrostructure of interfacial fracture surface; **b** Middle unbonded zone; **c** Low-waviness region; **d** Flat region with continuous melting near the unbonded zone showing

intragranular fracture; **e** Transition from high-waviness to low-waviness interface; **f** Magnified view of F zone in low-waviness region. The white arrow represents the wave transition direction

zone in the weld center, shown in Fig. 8a, b, appears darker than other areas since there was no weld formation in this area. Part of the jetted material remains at the initial collision point since the impact angle is zero. In the flat region near the unbonded zone (Fig. 8d), intergranular brittle fracture was found, and some areas entail cleavage facets. Figure 8c and f show the low-waviness interface with regular wave crest and trough. The waviness of the interface becomes higher when scanning from the unbonded zone to the trapped jet zone. Figure 8e shows the transition from high-waviness to low-waviness region. More severe tearing was shown in high-

waviness interfaces. Once the shear force is larger than the metallurgical bonding force of high-waviness area, cracks would proceed through this area and reach low-waviness region. Further fast propagation through the flat interface with continuous melting layer would occur, resulting in interfacial fracture.

Ti, Cr, and Fe are present in wave trough and crest regions as shown in Fig. 9, which indicates material transfer occurred on the low-waviness interface between Ti and SS [11]. Material transfer has been found in vaporizing foil actuator welding of other metal pairs as well such as Ti/Fe, Al/Fe,

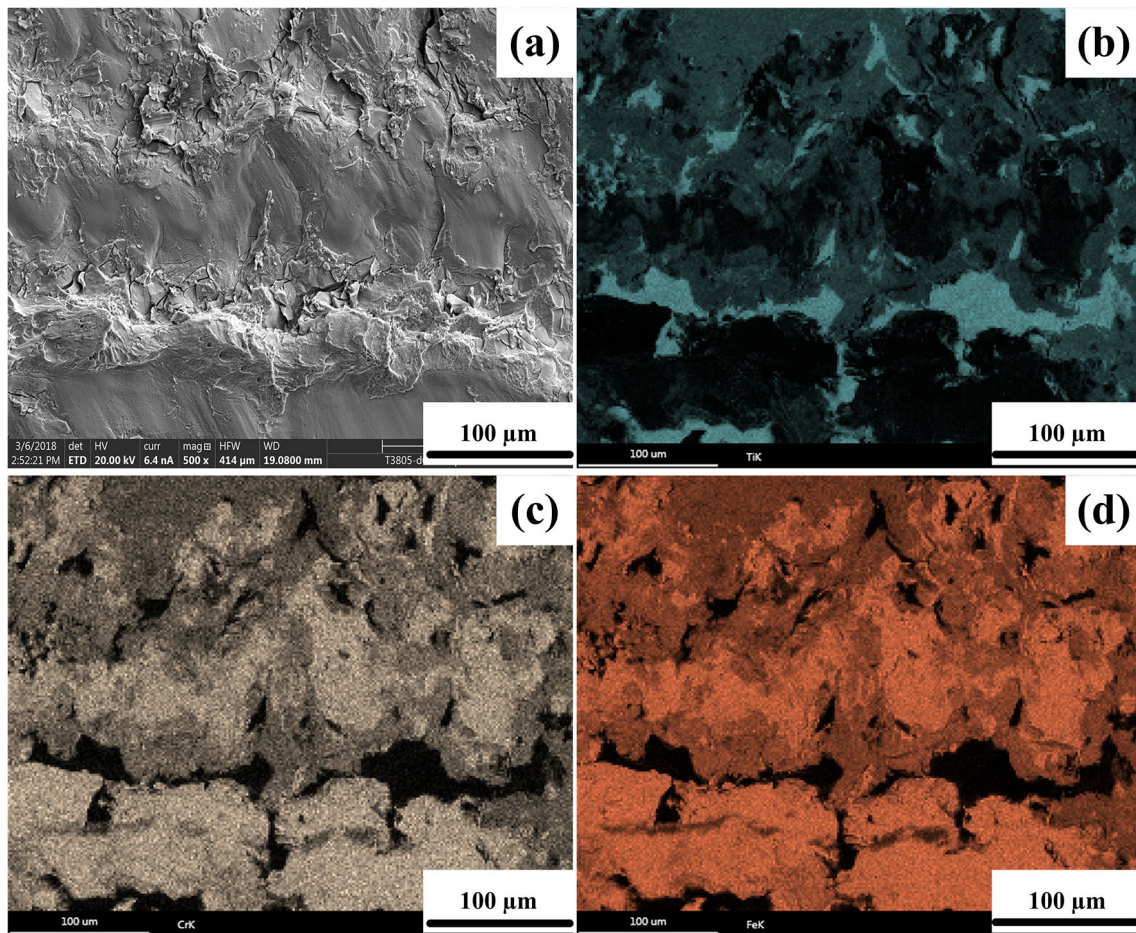


Fig. 9 EDS map of wavy fracture surface in Fig. 5f. **a** Wavy region; **b** Element distribution of Ti; **c** Element distribution of Cr; **d** Element distribution of Fe

and Al/Mg due to the severe plastic deformation involved in this high-velocity impact welding [14, 25, 26].

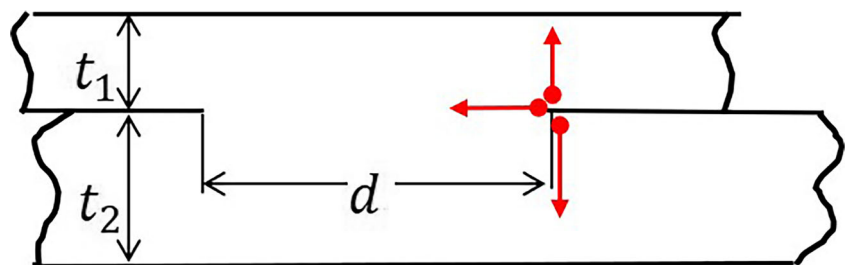
4.4 Quantitative analyses of VFA weld characteristics and failure modes

In using mesh-insensitive structural stress analysis method as described in Section 3, a spot weld between two sheets with a bonded region of diameter d (as illustrated in Fig. 10) possesses three potential failure modes at each interface notch location. Two corresponding cracks originating at the notch tip propagate through either the top sheet (i.e., t_1) or bottom sheet (t_2); the third one propagates along the bond line (along

d). Which failure mode becomes dominant mostly depends on weld size (d) and weld quality characteristics at the crack origin and along the crack path.

The application of such failure mode characterization for VFA spot weld discussed in the previous section was illustrated in Fig. 11 with respect to a typical weld macrograph, in which an unwelded central region (illustrated by the thick black line) is shown. This unwelded zone is induced by the normal impact during the welding process, as depicted in Fig. 2. As a result, three additional potential failure modes originating from the inner notch on the left should also be considered (the same can be done for the inner notch on the right). Based on the information, a three-dimensional solid element

Fig. 10 Typical failure modes in a spot weld



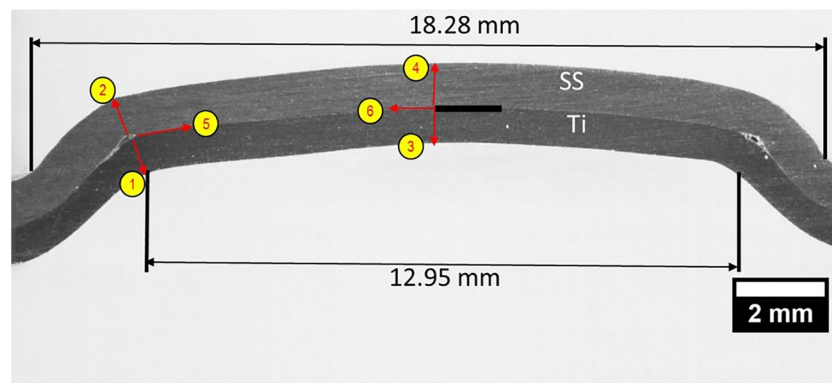


Fig. 11 Failure mode definition for VFA spot weld samples used in this study. Failure location 1: through-thickness failure at titanium sheet from the dimple edge; Failure location 2: through-thickness failure at stainless steel sheet from the dimple edge; Failure location 3: through-thickness

failure at titanium sheet from the unwelded zone; Failure location 4: through-thickness failure at stainless steel sheet from the unwelded zone; Failure location 5: interfacial failure from the dimple edge; Failure location 6: interfacial failure from the unwelded zone

model for modeling the lap shear specimen (Fig. 1) is shown in Fig. 12. ABAQUS was used to perform the linear elastic analysis for determining structural stress corresponding to each of the six failure modes indicated in Fig. 11. The element type is C3D8R. Boundary conditions were applied for two purposes. One is to fix the end of the stainless steel side by restricting all translations in X, Y, and Z of the global coordinate and the other is to simulate grip condition to both of the sheets by restricting movement in z-direction. Unit pressure was applied to the end of the titanium sheet as illustrated in Fig. 12b. The unwelded central region was modeled as shown in Fig. 12c, and its size (2 mm in diameter) is corresponding to the micrograph examined after the welding.

By following the structural stress calculation procedure described in Section 3, the through-thickness membrane stress σ_m and bending stress σ_b were calculated along the weld line for each failure locations identified in Fig. 11. Then the effective structural stress σ_e was calculated according to Eq. (2). The results were normalized by the remote nominal stress which is defined as the applied nominal stress on the titanium sheet (unit stress applied in this study) and summarized in Fig. 13. Therefore, the results in Fig. 13 represent the stress concentration effect. Figure 13a shows the circumferential variation of the effective stresses corresponding to each failure location, while Fig. 13b shows the peak stress for each failure location. The results in Fig. 13b suggest that sheet failure at

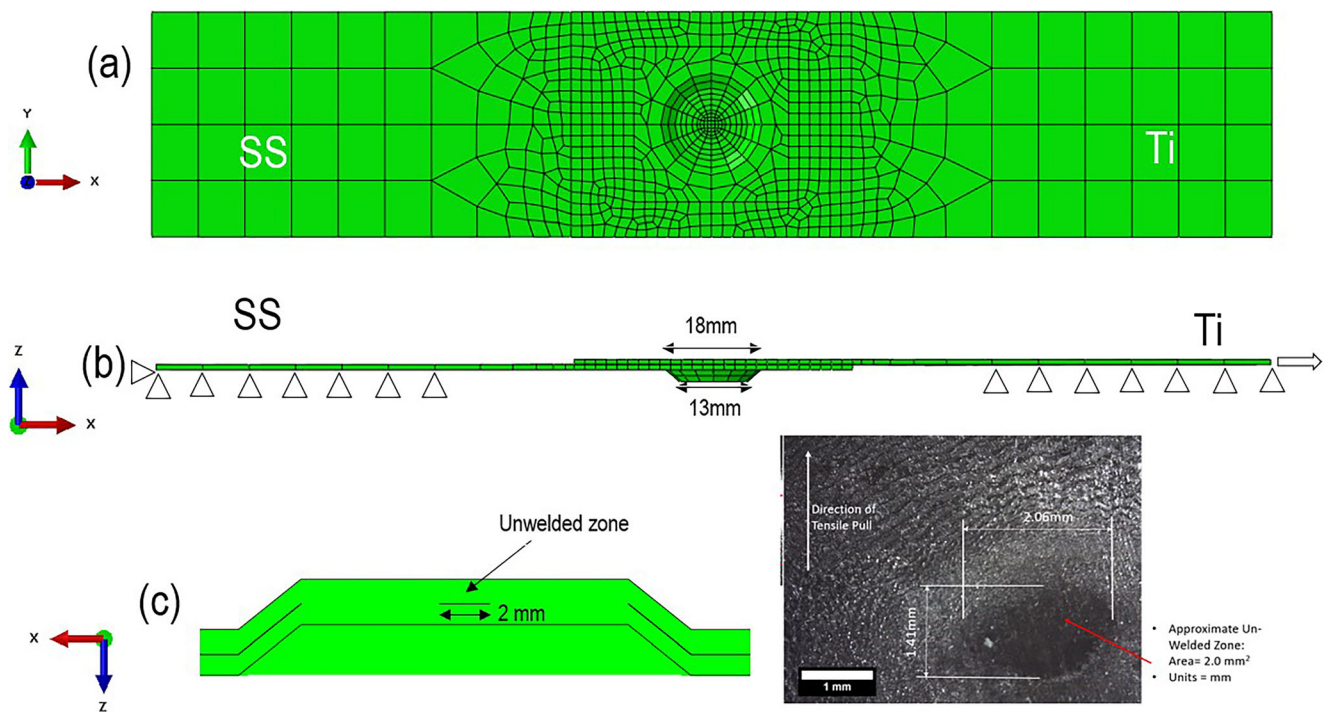
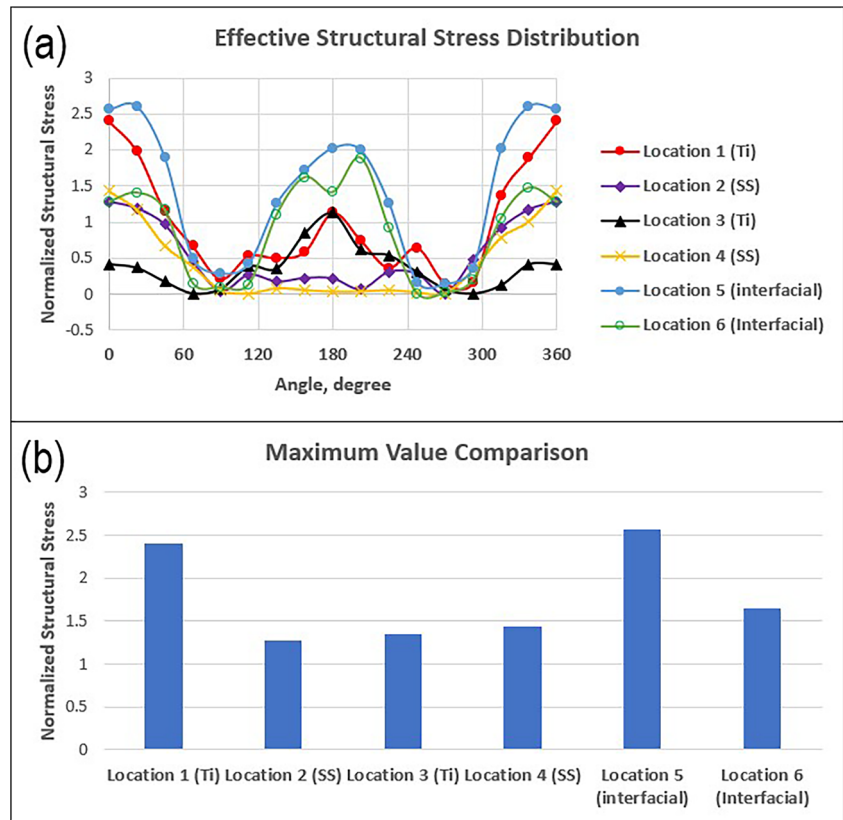


Fig. 12 3D finite element for lap specimen subjected to remote tension. **a** Top view of the 3D finite element model. **b** Side view of the 3D finite element model with boundary conditions and loading condition. **c** The unbonded line at the VFA weld nugget

Fig. 13 Comparison of calculated structural stress at different failure locations shown in Fig. 11. **a** Circumferential variation of the normalized opening stresses corresponding to each failure location; **b** Peak stress for each failure location identified from (a)



location 1 (cracking into the titanium sheet) and failure location 5 (interfacial cracking along the bonding line) are dominant and almost equally possible. This finding is also consistent with the experimental observations which shows the dominant failure modes are interfacial failure (location 5, IF) and pullout failure from the titanium sheet (location 1, N-Ti) in Section 4.2. As for which one will control the final failure, it is

dependent upon the bond line quality particularly in the areas of interfacial notch root and any deviation of actual bond line from what is assumed in the model shown in Fig. 12.

It is worth mentioning that the results for location 1 (around 2.4) shown in Fig. 13 are for nugget pullout failure at the dimple edge. As for the partial nugget pullout failure mode, it is noticed that the averaged failure location is about 2 mm away from the

Fig. 14 Partial pullout failure by considering 2-mm unbonded area from the dimple edge: **a** Failure picture, **b** unbonded line in the weld nugget, and **c** failure mode definition

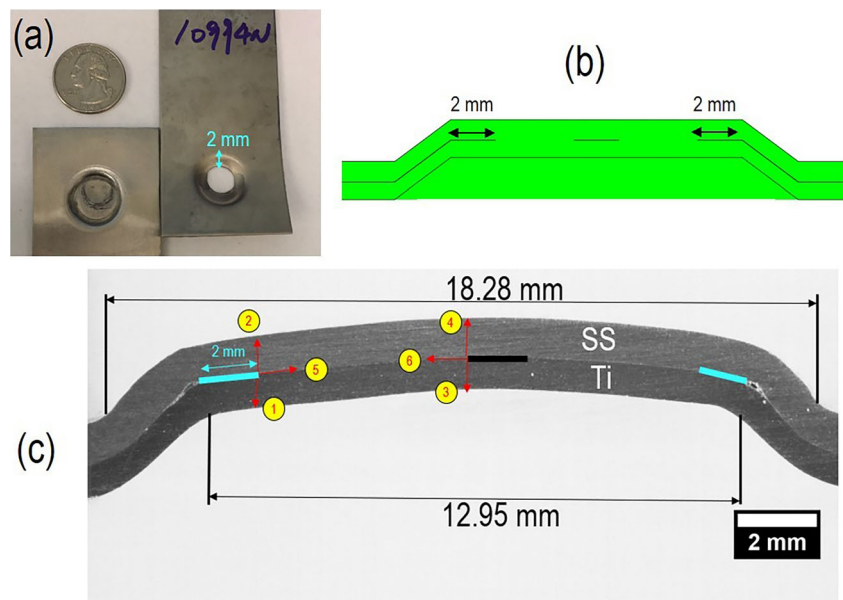
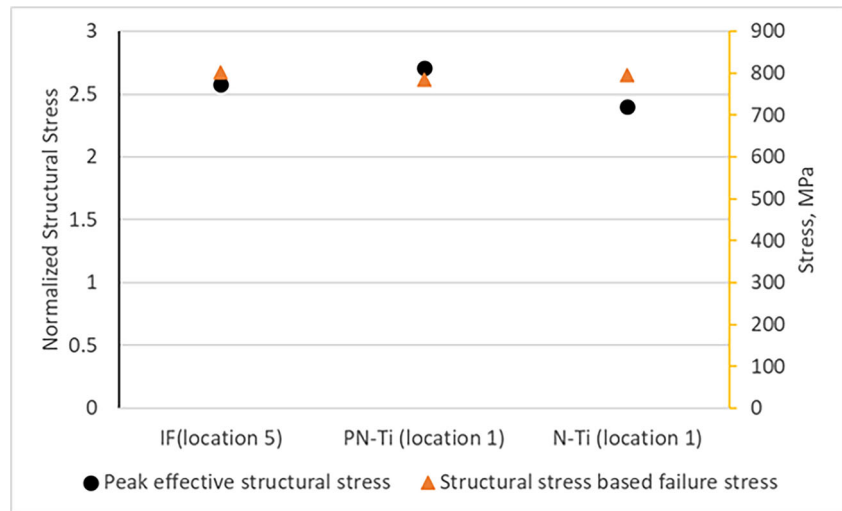


Fig. 15 Peak effective structural stress and data correlation using the peak effective structural stress for different failure modes: IF (location 5), PN-Ti (location 1 for partial pullout failure), and N-Ti (location 1 for pullout failure)



dimple edge, as shown in Fig. 14a. By considering the 2-mm characteristic length, both the FE model at the weld nugget and failure locations were changed correspondingly and depicted in Fig. 14 b and c, respectively. Then, following the same calculation procedure, the resultant peak effective structural stress at location 1 is 2.7 which shows a gradual increase in the stress concentration for the partial pullout failure.

Three dominant failure modes observed both in the experiments (Section 4.1) and analysis (Fig. 13) are interfacial fracture (IF, location 5 for pullout failure), partial nugget pullout failure from the titanium sheet (PN-Ti, location 1 for partial pullout failure), and nugget pullout failure from the titanium sheet (N-Ti, location 1 for pullout failure). Figure 15 summarized the corresponding peak effective structural stress $\sigma_{e, \max}$ (plotted in black). Nugget pullout failure from the SS side is abnormal (only one case) and needs further examination. Therefore, this failure mode is not considered in this section for the data analysis. The structural stress-based failure stress can be calculated by using the peak failure load in Fig. 5b to multiply the $\sigma_{e, \max}$ (resulting from the remote unit stress) given in Fig. 13b. The calculated results are plotted in orange triangles. In contrast to the significant

discrepancies in peak loads among different failure modes depicted in Fig. 15, there shows an improved correlation in failure stress without noticeable difference using the traction structural stress method. It implies that the failure stress is consistent for any failure mode.

The mesh-insensitive method can also be effectively used for determining the effects of the unwelded region in the spot weld center area. This can be demonstrated by introducing a slightly large unwelded area with diameter of 5 mm (see Fig. 16a). The results in Fig. 16b show that even if D is as large as 5 mm, it has no noticeable effects on stress concentration factors corresponding to the dominant failure modes (1 and 5). These results show that despite varied failure modes and nugget strength, strength itself is not usually affected adversely by the size of the central unbonded zone.

5 Discussion

As studied in the previous work [15], the impact velocity from 2.0 to 2.6 kJ has not seen significant variation since the energy

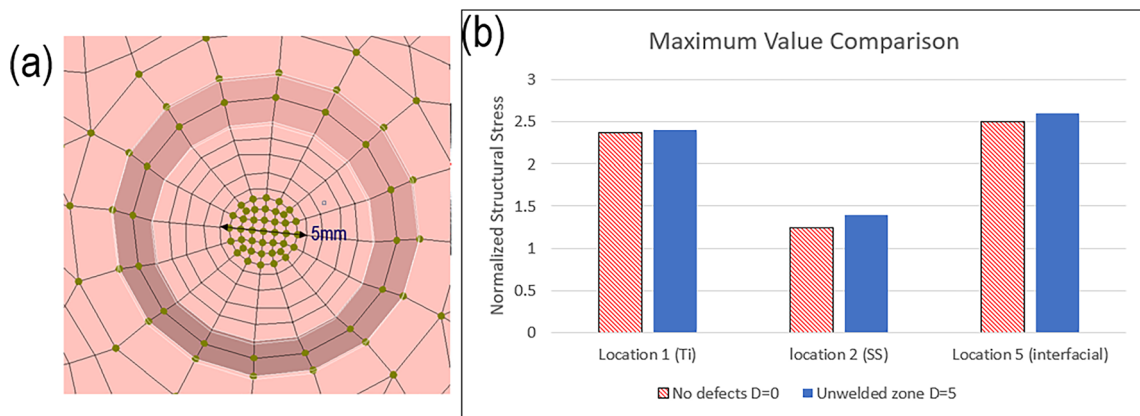
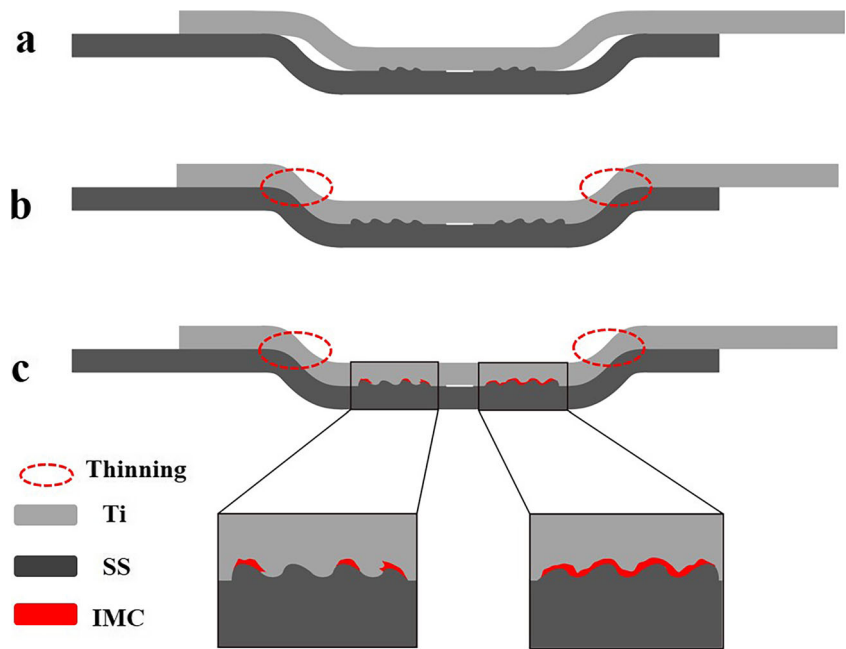


Fig. 16 Effect of the unbonded zone size in VFA spot weld. **a** Mesh; **b** Normalized structural stress at different locations with different size of unbonded zone

Fig. 17 Possible relationship between microstructures and failure modes after lap shear testing. **a** Incomplete joining, resulting in partial nugget pullout; **b** Little melting and minimal thinning on the welds, resulting in nugget pullout failure mode; **c** Mixture of discontinuous melting pockets and a continuous melting layer resulting in partial nugget pullout; continuous melting along the whole interface could result in interfacial fracture



deposition in the aluminum foil reaches the maximum limit in this input energy range. This insignificant impact velocity variation results in the minor change of interfacial macrostructures as shown in Fig. 4, and thus minimal change in the peak failure loads. But the varied failure modes occurred in these joints for two major reasons. One could be the by-hand nature of the experimental setup, normally aligning the aluminum foil actuator manually. The other is that the shape of the aluminum foil likely presents variations, resulting in inconsistent vaporization of the middle active area of the aluminum foil. This inconsistent vaporization leads to inconsistent plasma pressure which is the main driving force of VFA welding.

Aside from experimental setup issue, IMC distribution along the interface also plays an important role. In Crossland et al. [27] and Bataev et al. [28], the varied IMC distributions entail different effects on the mechanical properties. If these IMC exhibit as separate islands along the interface, their potential brittleness poses insignificant influence on the mechanical properties. Meanwhile, if these IMC are present continuously along the interface, their high brittleness will result in brittle fracture along the interface. Since no simultaneous testing on the microstructures and mechanical properties was done for the Ti/SS impact spot welds in this work, the exact relationship between microstructure and weld performance is difficult to reveal. However, possible mechanisms for the different failure modes can be explained in Fig. 17. Partial nugget pullout failure could result from incomplete joining (Fig. 17a) or a mixture of discontinuous melting pockets on one side and a continuous melting layer on the other side (Fig. 17c). Nugget pullout failure could result from little melting as well as minimal thinning at the edges (Fig. 17b), or only a small amount of discontinuous melting pockets distributed along the

interface. Still, there is no strong evidence for these proposed mechanisms for the failure modes observed in the spot impact welds. Based on the discussion in Section 4.4, the stress concentration conditions at the edges such as the unwelded zone near the edges and the low-waviness interfaces (Fig. 5) likely have an influence on the weld strength and failure modes, while the size of the unwelded zone in the weld center has insignificant influence on the failure modes.

6 Conclusions

Ti-1.2ASN alloy and 436 stainless steel were successfully joined by VFA welding at discharge energies ranging from 2 to 2.6 kJ. The microstructural characteristics and mechanical properties of Ti/SS VFA welds were summarized as follows:

1. Moving from center outwardly towards the edges, it was found that there is an unbonded zone in the center, a flat interface with continuous melting, a wavy interface with discontinuous melting, a wavy interface with no melting, and a trapped jet zone at the edges.
2. Multiple competing failure modes were found. Nugget pullout had the best mechanical performance and interfacial failure had the poorest. Even in the case of interfacial failure, there was strong evidence for metallurgical bonding, as demonstrated by material transfer.
3. In lap shear tests, nugget pullout failure mode can be achieved at a low input energy (2.2 kJ, or possibly less) for impact spot welding of Ti to SS. DIC result confirmed this failure mode by capturing the strain accumulation along the circumference.

4. A large scatter was observed in the absorbed energy during lap shear testing but small scatter in strength for different failure modes. The by-hand nature of the setup, the inconsistent vaporization of the aluminum foil, and the varied distribution of intermetallics along the interface are probably the three major reasons for the varied failure modes.
5. The VFA method shows great promise for joining titanium and stainless steel. While several failure modes were seen in this study, often failure was in base metal. If the process is properly controlled, it provides a promising way of dissimilar metal welding with joint strengths that exceed those of the base metal.
6. The mesh-insensitive structural stress method has been proven effective for estimating the most likely failure modes between nugget pullout and interfacial failure modes for VFA spot welds. The analysis results show that for a central unbonded region as large as 5 mm in diameter, both failure mode and nugget strength are not adversely affected.

Acknowledgements The authors would thank group members and colleagues from The Ohio State University for their kind help.

Funding information This work was supported by Lightweight Innovations for Tomorrow (LIFT). Project number and title are Joining-R2-1-60061248 and Development of Technologies for Joining Titanium to Steel, respectively. We are also thankful for support from National Science Foundation under a Major Research Instrument Grant No. 1531785.

Data availability The raw data used to reproduce the results cannot be completely shared due to an ongoing research along with this project. Part of the unpublished data will be attached as [supplementary materials](#).

Compliance with ethical standards

Conflict of interest The authors declare that they have no conflict of interest.

References

1. Gangwar K, Ramulu M (2018) Friction stir welding of titanium alloys: a review. *Mater Des* 141:230–255
2. Dey HC, Ashfaq M, Bhaduria AK, Prasad Rao K (2009) Joining of titanium to 304 L stainless steel by friction welding. *J Mater Process Technol* 209:5862–5870
3. Tomashchuk I, Grevey D, Sallamand P (2015) Dissimilar laser welding of AISI316L stainless steel to Ti6–Al4–6V alloy via pure vanadium interlayer. *Mater Sci Eng A* 622:37–45
4. Tomashchuk I, Sallamand P, Belyavina N, Pilloz M (2013) Evolution of microstructures and mechanical properties during dissimilar electron beam welding of titanium alloy to stainless steel via copper interlayer. *Mater Sci Eng A* 585:114–122
5. Muralimohan CH, Muthupandi V, Sivaprasad K (2014) Properties of friction welding titanium–stainless steel joints with a nickel interlayer. *Procedia Mater Sci* 5:1120–1129
6. Fazel-Najafabadi M, Kashani-Bozorg SF, Zarei-Hanzaki A (2010) Joining of CP-Ti to 304 stainless steel using friction stir welding technique. *Mater Des* 31:4800–4807
7. Kundu S, Chatterjee S (2006) Interfacial microstructure and mechanical properties of diffusion-bonded titanium–stainless steel joints using a nickel interlayer. *Mater Sci Eng A* 425:107–113
8. Akbari Mousavi SAA, Farhadi Sartangi P (2008) Effect of post-weld heat treatment on the interface microstructure of explosively welded titanium–stainless steel composite. *Mater Sci Eng A* 494:329–336
9. Manikandan P, Hokamoto K, Fujita M, Raghukandan K, Tomoshige R (2008) Control of energetic conditions by employing interlayer of different thickness for explosive welding of titanium/304 stainless steel. *J Mater Process Technol* 195:232–240
10. Chu Q, Zhang M, Li J, Yan C (2007) Experimental and numerical investigation of microstructure and mechanical behavior of titanium/steel interfaces prepared by explosive welding. *Mater Sci Eng A* 689:323–331
11. Mousavi SAAA, Sartangi PF (2009) Experimental investigation of explosive welding of cp- titanium/AISI 304 stainless steel. *Mater Des* 30:459–468
12. Hahn M, Weddeling C, Taber G, Vivek A, Daehn GS, Tekkaya AE (2016) Vaporizing foil actuator welding as a competing technology to magnetic pulse welding. *J Mater Process Technol* 230:8–20
13. Psyk V, Risch D, Kinsey BL, Tekkaya AE, Kleiner M (2011) Electromagnetic forming—a review. *J Mater Process Technol* 211:787–829
14. Vivek A, Hansen SR, Liu BC, Daehn GS (2013) Vaporizing foil actuator: a tool for collision welding. *J Mater Process Technol* 213:2304–2311
15. Li J, Schneiderman B, Gilbert SM, Vivek A, Yu Z, Daehn G (2020) Process characteristics and interfacial microstructure in spot impact welding of titanium to stainless steel. *J Manuf Process* 50:421–429
16. Kapil A, Lee T, Vivek A, Cooper R, Hetrick E, Daehn G (2019) Spot impact welding of an age-hardening aluminum alloy: process, structure and properties. *J Manuf Process* 37:42–52
17. Kapil A, Lee T, Vivek A, Bockbrader J, Abke T, Daehn G (2019) Benchmarking strength and fatigue properties of spot impact welds. *J Mater Process Technol* 255:219–233
18. Nassiri A, Vivek A, Abke T, Liu B, Lee T, Daehn G (2017) Depiction of interfacial morphology in impact welded Ti/Cu bimetallic systems using smoothed particle hydrodynamics. *Appl Phys Lett* 110:231601
19. Dong P (2001) A structural stress definition and numerical implementation for fatigue analysis of welded joints. *Int J Fatigue* 23(10):865–876
20. Kang HT, Dong P, Hong JK (2007) Fatigue analysis of spot welds using a mesh-insensitive structural stress approach. *Int J Fatigue* 29(8):1546–1553
21. Lu H, Dong P, Boppudi S (2015) Strength analysis of fillet welds under longitudinal and transverse shear conditions. *Mar Struct* 43:87–106
22. Dong P, Hong JK, Osage DA, Dewees DJ, Prager M (2010) The master SN curve method an implementation for fatigue evaluation of welded components in the ASME B&PV Code. Section VIII, Division 2 and API 579-1/ASME FFS-1. *Weld Res Council Bull*:523
23. Wang P, Pei X, Dong P, Song S (2019) Traction structural stress analysis of fatigue behaviors of rib-to-deck joints in orthotropic bridge deck. *Int J Fatigue* 125:11–22
24. Dong P, Pei X, Xing S, Kim MH (2014) A structural strain method for low-cycle fatigue evaluation of welded components. *Int J Press Vessel Pip* 119:39–51
25. Liu B, Vivek A, Presley M, Daehn GS (2018) Dissimilar impact welding of 6111-T4, 5052-H32 aluminum alloys to 22MnB5,

- DP980 steels and the structure–property relationship of a strongly bonded interface. *Metall Mater Trans A* 49:899–907
26. Liu B, Vivek A, Glenn GS (2017) Joining sheet aluminum AA6061-T4 to cast magnesium AM60B by vaporizing foil actuator welding: input energy, interface, and strength. *J Manuf Process* 30: 75–82
 27. Crossland B (1992) Explosive welding of metals and its application
 28. Bataev IA, Lazurenko DV, Tanaka S, Hokamoto K, Bataev AA, Guo Y, Jorge AM Jr (2017) High cooling rates and metastable phases at the interfaces of explosively welded materials. *Acta Mater* 135:277–289

Publisher's note Springer Nature remains neutral with regard to jurisdictional claims in published maps and institutional affiliations.